Article

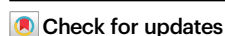# Gradient area-selective deposition for seamless gap-filling in 3D nanostructures through surface chemical reactivity control

Chi Thang Nguyen[1,5], Eun-Hyoung Cho[2,5], Bonwook Gu[1], Sunghee Lee[2], Hae-Sung Kim[2], Jeongwoo Park[3], Neung-Kyung Yu[3], Sangwoo Shin[4], Bonggeun Shong[3], Jeong Yub Lee[2] & Han-Bo-Ram Lee[1] ✉

The integration of bottom-up fabrication techniques and top-down methods can overcome current limits in nanofabrication. For such integration, we propose a gradient area-selective deposition using atomic layer deposition to overcome the inherent limitation of 3D nanofabrication and demonstrate the applicability of the proposed method toward large-scale production of materials. $Cp(CH_3)_5Ti(OMe)_3$ is used as a molecular surface inhibitor to prevent the growth of TiO_2 film in the next atomic layer deposition process. $Cp(CH_3)_5Ti(OMe)_3$ adsorption was controlled gradually in a 3D nanoscale hole to achieve gradient TiO_2 growth. This resulted in the formation of perfectly seamless TiO_2 films with a high-aspect-ratio hole structure. The experimental results were consistent with theoretical calculations based on density functional theory, Monte Carlo simulation, and the Johnson-Mehl-Avrami-Kolmogorov model. Since the gradient area-selective deposition TiO_2 film formation is based on the fundamentals of molecular chemical and physical behaviours, this approach can be applied to other material systems in atomic layer deposition.

Decades ago, top-down and bottom-up approaches were competitively studied for next-generation nanoscale fabrication. The top-down approach, which is primarily used for the nanofabrication of Si devices using photolithography and etching, has been recently used to fabricate 3D nanostructures, such as nanowires and nanodots, which were previously only obtainable through the bottom-up approach. The top-down approach also facilitates large-scale manufacturing, which has allowed this approach to dominate the current nanofabrication technology. Top-down-approach-based nanofabrication is essential for the construction of modern Si electronics and other devices, such as biomedical and energy devices. In addition, many challenges that limit top-down-approach-based nanofabrication have been resolved by realising an integrated approach incorporating the bottom-up

technology. An example of such an integrated approach is area-selective deposition (ASD) that is based on surface chemical reactivity control.

Atomic layer deposition (ALD) enables nanoscale precise thickness control, excellent uniformity and conformality because of the unique surface self-saturated reactions of precursors and counter-reactants[1-3]. Because ALD allows strong surface-dependent growth, a film could be selectively deposited on a specific area to achieve chemical reactivity control. Self-assembled monolayers, organic molecules, polymers and ALD precursors have been introduced to inhibit or promote the surface chemical reactivity of ASD-grown films[4-7]. An inhibitor selectively adsorbs on a specific surface and inhibits the subsequent ALD growth on the surface only, allowing bottom patterns

[1]Department of Materials Science and Engineering, Incheon National University, Incheon 22012, Korea. [2]Beyond Silicon Lab, Samsung Advanced Institute of Technology, Gyeonggi 16678, Korea. [3]Department of Chemical Engineering, Hongik University, Seoul 04066, Korea. [4]Department of Mechanical and Aerospace Engineering, University at Buffalo, Buffalo, NY 14260, USA. [5]These authors contributed equally: Chi Thang Nguyen, Eun-Hyoung Cho. ✉e-mail: hbrlee@inu.ac.kr

to transfer to upper patterns through ASD. For example, in our previous study[8], ASD was conducted using a Si precursor inhibitor that was previously used for the ALD of SiO$_2$. The study highlighted that the Si precursor inhibitors selectively adsorbed on a OH-terminated SiO$_2$ surface but not on a H-terminated Si surface, inhibiting the growth of Pt and Ru ALD. Until now, most ASD-based research has focused on the selective growth between two different surfaces such as SiO$_2$/Si, SiO$_2$/Cu and SiO$_2$/HfO$_2$ for expanding the application scope of ASD in material fabrication and on the adsorption selectivity of inhibitors[8–12]. If the growth selectivity in ASD can be controlled using other factors, such as the geometry of nanopatterns, but not by surface termination, then ASD can be extended to other bottom-up-approach-based applications to overcome the limits impeding nanofabrication.

Isotropic growth is the main advantage of ALD; however, such growth induces the negative side effect of seam and void formation in high-aspect-ratio 3D structures such as holes and trenches[13]. As the number of ALD cycles increases, structure openings become closed (pinch-off) at a certain film thickness, forming voids or seams along the centreline as shown in Fig. 1a. The seams and voids are unavoidable critical defects formed during nanofabrication; they degrade device performance, electrical conductivity and thermal or mechanical properties[14–16]. To avoid seam formation, anisotropic growth inside the structure, like V-shaped growth, is required but cannot be achieved from the isotropic growth during ALD (Fig. 1b)[14].

Seamless deposition of TiO$_2$ in 3D nanostructures is essential for optical device applications, such as the fabrication of metasurfaces[17,18], but there is no proper deposition method to realize it[19,20]. In this study, we introduce a process of gradient ASD of a TiO$_2$ film that allows seamless gap-filling; the process is illustrated in Fig. 1c. Through ALD, a TiO$_2$ film is deposited on high-aspect-ratio (AR) hole patterns; a Ti inhibitor layer is then adsorbed onto this TiO$_2$ film. The adsorption densities of the inhibitor vary depending on the geometrical positions and induce different blocking properties in the inhibitor. This causes ALD-grown TiO$_2$ films to grow anisotropically, resulting in gap-filling without seam formation and realising the above-mentioned objective of the proposed gradient ASD concept. To inhibit TiO$_2$ growth, herein, a Ti inhibitor is introduced, namely, trimethoxy-(pentamethylcyclopentadienyl)-titanium(IV) [TMPMCT], which was originally developed as a Ti precursor for ALD TiO$_2$. TMPMCT-inhibited film growth and seamless gap-filling were investigated

using various experimental and theoretical methods, including density functional theory (DFT) calculation, Monte Carlo (MC) simulation and the Johnson–Mehl–Avrami–Kolmogorov (JMAK) model. Initial experiments of gradient ASD were demonstrated in a lab-scale ALD system, and its wafer-scale demonstration was performed in a production-scale spatial-divided ALD system. Based on this research, we believe that the proposed approach can be applied for the ALD-assisted fabrication of other material systems.

Results

Previous reports suggest that TMPMCT is only oxidised by reactive oxidants, such as ozone and O$_2$ plasma[21,22], but not by H$_2$O[23,24]. Thus, if TMPMCT covers a surface before an ALD process using a H$_2$O counter-reactant, TMPMCT could inhibit the subsequent ALD growth by assuming no reaction between TMPMCT and the ALD precursor. This study used TMPMCT to inhibit subsequent TiO$_2$ ALD using a tetrakis(dimethylamido)titanium (TDMAT) precursor and a H$_2$O counter-reactant and investigated the adsorption stability of TMPMCT upon TDMAT and H$_2$O exposure. In the DFT results in Fig. 2a, the molecular configuration of TMPMCT after adsorption indicates that the OMe ligands create bonds with the TiO$_2$ surface and the Cp(CH$_3$)$_5$ ligand faces the outer surface. Adsorption of TMPMCT on the TiO$_2$ surface is assumed to be dissociative adsorption via removal of individual OMe ligands as shown in Fig. 2a. A detailed description of the reaction mechanism is suggested in Supplementary Note 1. The adsorption of TMPMCT can be considered facile, as it is exothermic and does not involve significant activation energy. Then, when the surface becomes saturated by adsorbed TMPMCT, the outer surface would become terminated by the Cp(CH$_3$)$_5$ ligands. These cyclopentadienyl ligands with low chemical reactivity[24–26] can then hinder the adsorption of subsequent TDMAT precursors.

Figure 2b shows the water contact angle (WCA) of the TMPMCT/TiO$_2$ surface as a function of TMPMCT exposure time. While the WCA of the hydrophilic TiO$_2$ surface[27–29] was 45.1° before exposure to TMPMCT, it rapidly increased to 83.0° and 97.7° after 10 s and 60 s exposure of TMPMCT, respectively. The increase in WCA is attributed to the formation of a chemically inert surface resulting from the Cp(CH$_3$)$_5$Ti-ligand-terminated surface, as observed from the DFT results. No change of TiO$_2$ thickness was observed after the reaction between TMPMCT and H$_2$O (see Supplementary Fig. 1e), indicating TMPMCT is stable under H$_2$O exposure. The blocking property of TMPMCT against 1000 cycles of ALD TiO$_2$ was evaluated at different TMPMCT exposure times. Figure 2c shows that TiO$_2$ growth on a TMPMCT-free surface is linear as a function of the ALD cycles. In contrast, there is almost no TiO$_2$ film growth on the 20 s TMPMCT inhibition layer, the growth exhibits linearity as in the TMPMCT-free sample after 200 cycles. The TiO$_2$ ALD film growth is inhibited for up to 700 and 900 cycles for the 40 s (blue points with error bars) and 60 s TMPMCT (orange points with error bars) inhibition layers, respectively. Then the TiO$_2$ ALD film growth is linear as in the case of 20 s TMPMCT inhibition layer. The selectivity is calculated from the thickness measured by ellipsometry (Fig. 2c) and the results are shown in Fig. 2d. At small numbers of TiO$_2$ ALD cycles, the deposit amount significantly affects the selectivity. In addition, ellipsometry has errors in the scale of a few angstroms, resulting in large deviations in the calculated selectivity for low-thickness films. However, separate SEM and TEM results (Supplementary Fig. 2) revealed that there was almost no growth of the TiO$_2$ ALD thin film on 60 s TMPMCT/SiO$_2$ (Supplementary Fig. 2a) and 60 s TMPMCT/10 nm TiO$_2$/SiO$_2$ (Supplementary Fig. 2b). Figure 2d indicates a very high calculated selectivity of >90% even after 900 cycles that is identical to the blocking of a 45-nm TiO$_2$ thin film. The inhibition of the TiO$_2$ film growth (using the same TDMAT precursor) herein was compared with that in the literature (Supplementary Table 1). The largest thickness of the inhibited TiO$_2$ film was 50 nm, achieved using a 43 nm poly(methylmethacrylate)
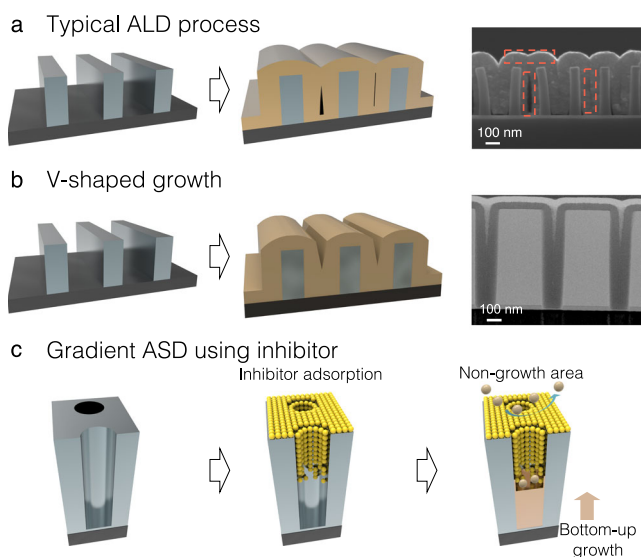

Fig. 1 | Schematic illustrations of ASD processes for seamless gap-filling.
a Typical ALD process. **b** ALD process for V-shaped growth. **c** The proposed gradient ASD process using an inhibitor.
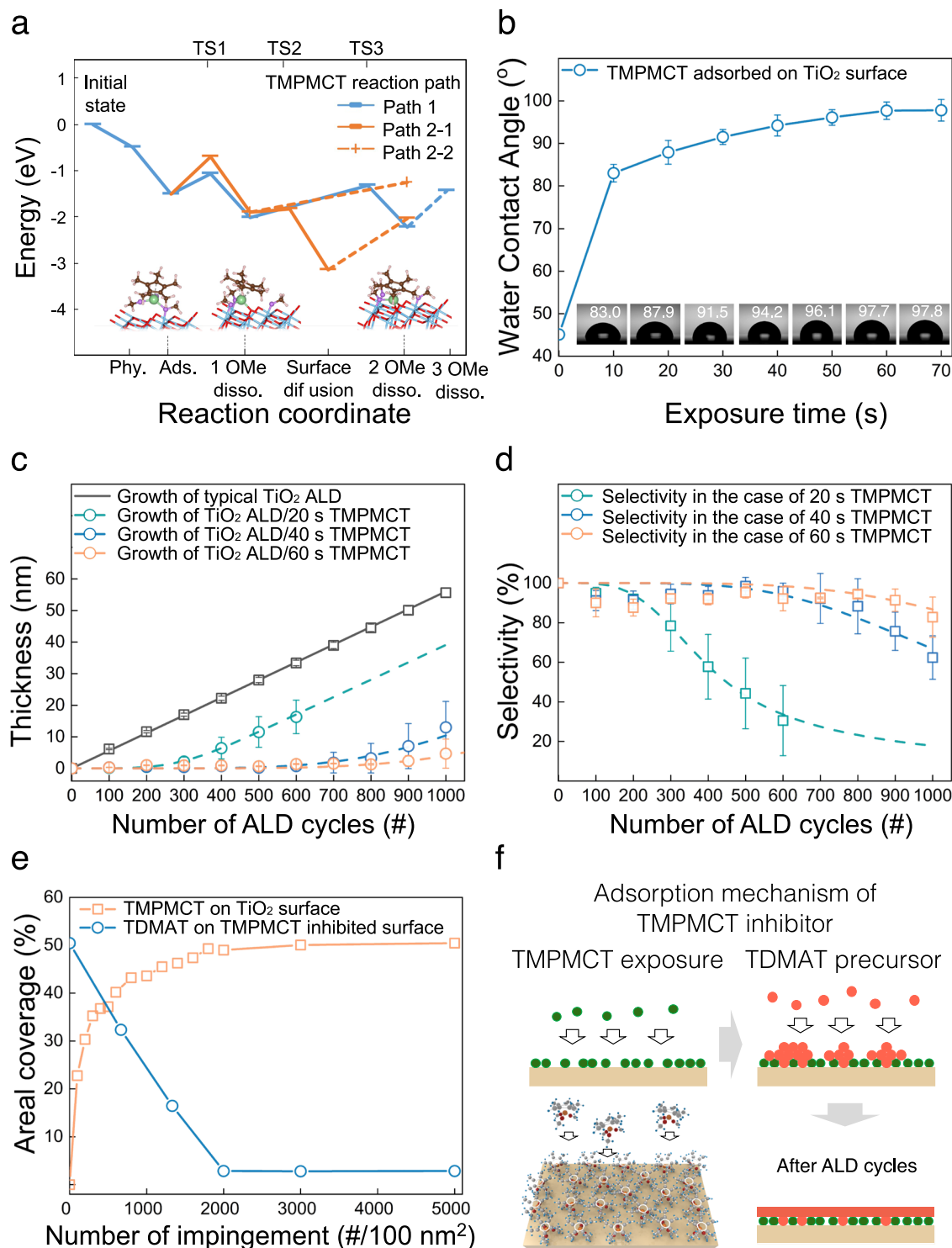
The figure panels are labelled:
a Typical ALD process
b V-shaped growth
c Gradient ASD using inhibitor (with labels: Inhibitor adsorption, Non-growth area, Bottom-up growth). Scale bars: 100 nm.

Fig. 2 | Adsorption behaviour and blocking property of TMPMCT inhibitor.
a Surface reaction energy diagram of TMPMCT molecules on the TiO_2 surface calculated by DFT. The structures below correspond to the Path 1. The dotted lines represent the reactions, where TS (transition states) structures were not calculated. Colours: Ti_{surf} (light blue), Ti_{TMPMCT} (yellow green), O_{surf} (red), O_{TMPMCT} (purple), C (brown), H (white pink). The corresponding chemical equations: Phy.: $Cp(CH_3)_5Ti(OMe)_3$, Ads.: $*-Cp(CH_3)_5Ti(OMe)_3$, 1OMe disso.: $*-Cp(CH_3)_5Ti(OMe)_2 + *-(OMe)$, 2OMe disso.: $*-Cp(CH_3)_5Ti(OMe) + 2-*-(OMe)$, 3OMe disso.: $*-Cp(CH_3)_5Ti + 3-*-(OMe)$. Phy. (Physisorption), Ads. (Adsorption), disso. (dissociation), surf (surface), * refers to adsorbed species. **b** WCA

measurement with various exposure times of TMPMCT on the TiO_2 surface. Fitting of the JMAK model (dashed lines) to the data (points with error bars) obtained from **c** the growth of subsequent TiO_2 ALD on the TMPMCT inhibitor layer (20, 40 and 60 s), and **d** selectivity calculated from the thickness measured by ellipsometry. **e** Areal coverage of TMPMCT on the TiO_2 surface (10 nm × 10 nm) using various impingement numbers calculated by MC simulation and the coverage of TDMAT on the TMPMCT-inhibited surface. **f** Adsorption mechanism of TMPMCT inhibitor. Unoccupied sites serve as starting points for the nucleation sites of TiO_2 in subsequent ALD cycles. Source data are provided as a Source data file.

inhibition layer[30], followed by 48 nm, achieved using a 76 nm poly-norbornene inhibition layer[7]. Comparatively, a single inhibitor layer was sufficient to inhibit the TiO_2 film growth to up to 45 nm in this study.

Once the TiO_2 surface was exposed to TMPMCT, the OH-terminated TiO_2 surface changed to a $Cp(CH_3)_5Ti$-terminated surface, and there was no significant reaction between the $Cp(CH_3)_5Ti$-terminated surface and Ti precursors, as expected based on the DFT calculation (see Supplementary Fig. 3). The maximum blocking cycle increased with increasing TMPMCT exposure time. Interestingly, the nucleation of subsequent TiO_2 occurred over this specific cycle, leading to the degradation of the blocking property. Two possible reasons for this could be considered: (1) a direct reaction of the $Cp(CH_3)_5Ti$-terminated surface and Ti precursor over a larger number of cycles and (2) the nucleation of TiO_2 on the defects in the TMPMCT inhibition layer. The DFT results eliminate the first reason. Therefore, we studied the nucleation of TiO_2 on the inhibited layer using the theoretical simulations and experimental approaches described below.

Employing the previously-developed MC simulation, we investigated the physical adsorption and coverage of TMPMCT[8,12,31] by only considering the physical steric hindrance of TMPMCT on a surface and using the adsorption configuration from the DFT calculation. Figure 2e depicts the areal coverages of TMPMCT on the TiO_2 surface and TDMAT on the TMPMCT-inhibited surface. The area coverage of TMPMCT on the bare TiO_2 surface rapidly increases with increasing TMPMCT impingement (orange line) and reaches a plateau of ~50%. Therefore, the coverage of subsequent TDMAT on the TMPMCT-covered surface gradually decreases (blue line). Although the coverage of TMPMCT on the TiO_2 surface is saturated, some unoccupied adsorption sites remain. TMPMCT could not completely occupy the sites because of steric hindrance, and the TDMAT precursor can adsorb even on the TMPMCT-saturated surface (Supplementary Fig. 4). This result suggests that unoccupied sites, which are potential nucleation sites in the subsequent ALD process, exist even on the fully saturated TMPMCT layer. Therefore, the blocking property is degraded over specific cycles due to nucleation on unoccupied sites, as shown in Fig. 2f. This is consistent with our observations from Fig. 2c and d. In addition, an interesting finding is that the number of unoccupied sites changed with increased exposure time at the beginning, which may explain the different blocking properties of the Ti inhibitor witnessed during different exposure times.

Because TiO_2 nucleates only on the defects of the inhibition layer, island growth occurs based on the Volmer–Weber island growth mode in the subsequent ALD process[32–34]. To understand the degradation process quantitatively, we adopted a kinetic model based on the Johnson–Mehl–Avrami–Kolmogorov (JMAK) model[4,35,36] (details in Supplementary Note 2, Supplementary Fig. 5). Based on the best fit results, the parameters including $\dot{G}$, $\dot{N}_0$ and v_d are listed in Supplementary Table 1, and the fitting results with the experimental data are plotted in Fig. 2c and d (dashed lines). Figure 2c depicts an high goodness of fits for the thickness vs. ALD cycle number data of 0.933, 0.908 and 0.939 for 20 s, 40 s and 60 s of exposure time, respectively. Similarly, the selectivity data exhibits a highly consistent fit, as depicted in Fig. 2d. In addition, the nuclei density and nucleation growth of TiO_2 on the inhibited surface by 20 s, 40 s and 60 s TMPMCT were simulated using the JMAK model (Supplementary Table 2 and Supplementary Fig. 6).

In fact, the defect of the inhibition layer is the OH-terminated original TiO_2 surface; hence, ALD TiO_2 easily nucleates on the defect sites during ALD if a defect site is still available. We assumed that the nucleation site density starts at 0 on the inhibition layer for JMAK simulation under ideal circumstances. Thus, the different nucleation site generation rates, $\dot{N}_0$ (presented in Supplementary Table 2) could be attributed to the different nucleation rates of TiO_2 caused by the different defect densities in the TMPMCT inhibitor layer. The higher

defect density caused by shorter inhibitor exposure results in a higher nucleation site density and reflects faster nucleation than that of lower defect density samples. In addition, the number of nucleation delay cycles resulting from the fitting are 80, 620 and 800 cycles for 20, 40 and 60 s, respectively. In an ideal ALD process, the precursor chemisorbs onto the potential sites or surface. If the surface species or termination is not highly reactive towards the precursor, it should be converted to a high-reactivity surface termination during the following reactant exposure time. The time required for low-to-high-reactivity conversion of the surface may affect the nucleation delay. For instance, H-terminated Si surface is not highly reactive toward the adsorption of tetrakis(dimethylamino)-hafnium (TDMAH) precursor; however, the surface can be converted to a OH-terminated Si surface via H_2O counter reactant exposure or an O-terminated Si surface via O_3 reactant pulsing, which exhibits high reactivity towards the TDMAH precursor[37]. In this study, this reason can be ruled out because the potential adsorption site for the next TDMAT precursor is the defect site, which is also the original TiO_2 surface. When a TMPMCT inhibitor is used, the coverage of TMPMCT limits the potential adsorption site of the next TDMAT precursor, forming a sub-monolayer after each cycle. The time required for monolayer formation from a sub-monolayer can drive the nucleation delay. Thus, the slower nucleation rate observed on the longer-TMPMCT exposure sample leads to the longer nucleation delay, as simulated.

A theoretical interpretation of the experimental results suggests that the control of unoccupied sites, which are the same as defect sites, is the most important factor for a higher blocking property. The DFT results showed that the TMPMCT chemisorbs onto the TiO_2 surface by releasing OMe ligands, but not all OMe ligands are dissociated. If the OMe ligand could also be eliminated, additional space would be available for the formation of the inhibitor, as depicted in Fig. 3a. Although the TMPMCT is not fully oxidised to TiO_2 by an H_2O reactant because of the remaining $Cp(CH_3)_5$ ligands, H_2O can further eliminate the OMe ligands through a hydrolysis reaction with the adsorbed TMPMCT[38]. The DFT calculation modelled a reaction of H_2O molecules with OMe ligands of the adsorbed TMPMCT and releases MeOH by-product, resulting in the formation of $Cp(CH_3)_5Ti(OMe)_{3-x}(OH)_x$ ($x = 0$, 1, 2 and 3). The energy for the ligand–exchange reaction between OMe and OH from H_2O on the surface according to the number of H_2O molecules is presented in Fig. 3b. Two adsorption configurations are considered due to a large degree of freedom, Config A and Config B. Both configurations show a decrease in E_{ad} as the more OMe ligands are modified into OH. From MC simulations for the adsorption of $Cp(CH_3)_5Ti(OMe)_{3-x}(OH)_x$ molecules, the results, shown in Fig. 3c, indicate that the point coverage of $Cp(CH_3)_5Ti(OMe)_{3-x}(OH)_x$ increased from 6.0% (without additional H_2O and remaining 3OMe ligands) to 6.6%, 6.9% and 7.2% while eliminating 1OMe, 2OMe and 3OMe ligands, respectively. Thus, from the theoretical calculations, an additional H_2O pulse can create more space for additional inhibitor adsorption, increasing the inhibitor coverage and decreasing the defect sites.

We modified the single 20 s TMPMCT pulse into two 10 s TMPMCT pulses disrupted by a 2.5 s pulse of H_2O and the single 40 s TMPMCT pulse into two 20 s TMPMCT pulses disrupted by a 5 s pulse of H_2O (Supplementary Fig. 7). We then evaluated their blocking properties up to 1000 cycles of ALD, as shown in Fig. 3d–g. As shown in Fig. 2, the TiO_2 growth was inhibited for up to 200 and 700 cycles under 20 s and 40 s TMPMCT exposure conditions, respectively. With additional H_2O exposure, however, the TiO_2 growth was inhibited for up to 400 and 900 cycles for 20 s and 40 s samples, respectively, as shown in Fig. 3d–g. The fitting results with the JMAK model showed high goodness of fits as shown in Fig. 3d–g. From the parameters obtained from the fittings (Supplementary Table 3), the decrease in the nucleation site generation rate, $\dot{N}_0$, and the increase in the nucleation delays, v_d, reflect an increase in the TMPMCT coverage by addition
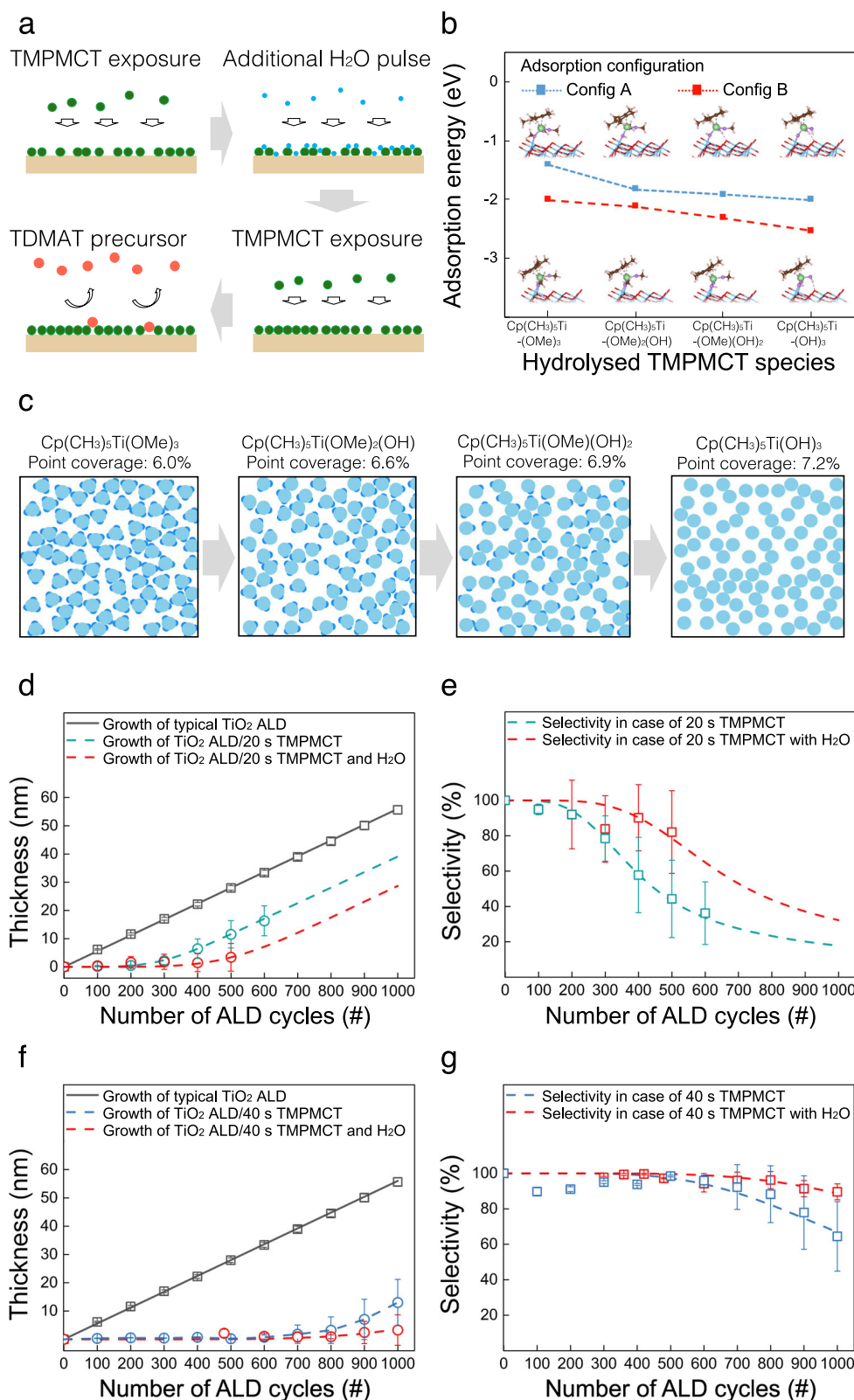
Fig. 3 | Blocking property of TMPMCT with an additional H_2O pulse. a Schematic of TMPMCT exposure with an additional H_2O pulse to improve coverage. **b** Adsorption energy of hydrolysed TMPMCT species, $Cp(CH_3)_5Ti(OMe)_{3-x}(OH)_x$ (x = 0, 1, 2 and 3), calculated by DFT. **c** MC simulation results for the adsorption of $Cp(CH_3)_5Ti(OMe)_{3-x}(OH)_x$ with steric hindrance in cases x = 1, 2 and 3. Fitting of the JMAK model to data (points with error bars) obtained from **d** growth and **e** selectivity in the case of 20 s TMPMCT with and without additional H_2O pulse samples. Fitting of the JMAK model to data (points with error bars) obtained from **f** growth and **g** selectivity in the case of 40 s TMPMCT with and without additional H_2O pulse samples. Source data are provided as a Source data file.
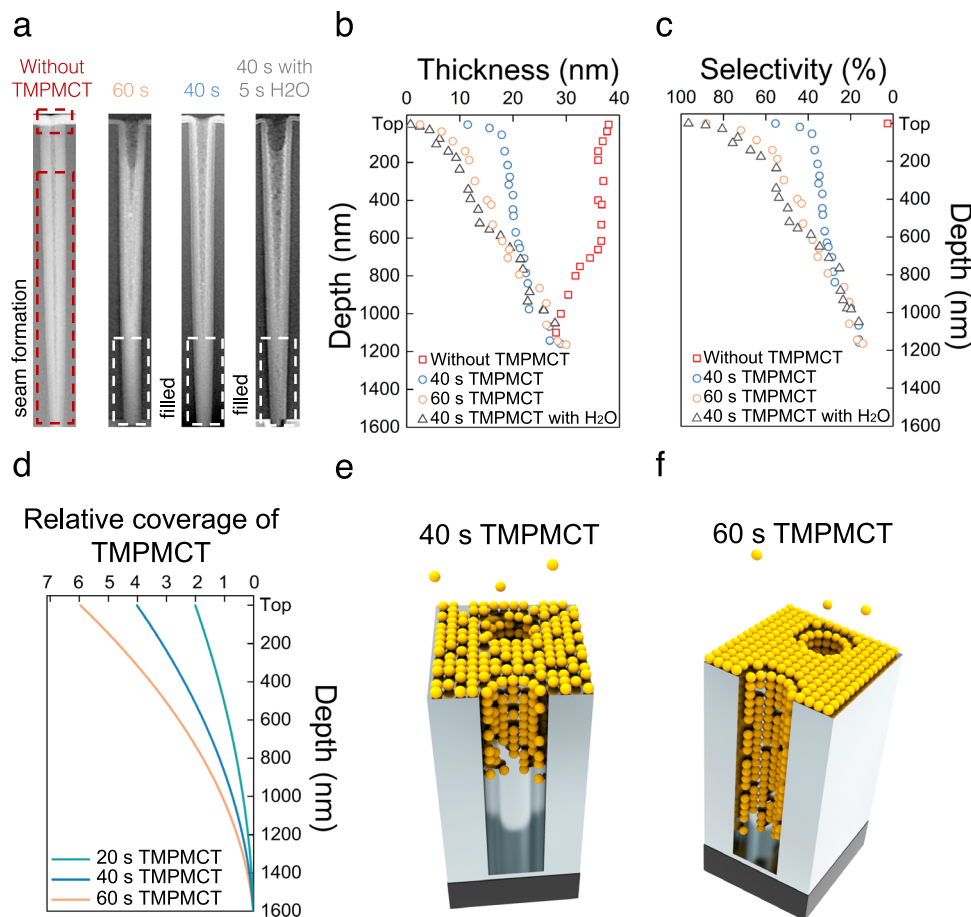
Fig. 4 | Hole pattern with a depth of 1600 nm, an opening diameter of 100 nm and a bottom diameter of 50 nm used for gap-filling. a TEM images of the subsequent 40 nm thick TiO$_2$ ALD film on the 0, 40 and 60 s TMPMCT inhibitors and 40 s TMPMCT with an additional H$_2$O/10 nm TiO$_2$/SiO$_2$ hole. **b** Growth and **c** selectivity calculated from the TEM results. **d** Relative coverage of various TMPMCT pulses, as calculated from the equation described in Supplementary Note 3 and depicted in illustrations **e** 40 s TMPMCT pulse, **f** 60 s TMPMCT pulse. Source data are provided as a Source data file.

H$_2$O, which leads to the reduction of defect sites, as predicted by DFT calculations and MC simulations.

From the results, we investigated different inhibitor coverages in a deep nanoscale hole pattern. We performed experiments on 8-inch wafers in a spatially divided ALD system, which has a high-volume manufacturing capability (Supplementary Fig. 8). We used 730 cycles of ALD on this nanoscale hole pattern to form a 40 nm thick TiO$_2$ layer, based on the growth per cycle (GPC) of TiO$_2$. As shown in Fig. 4a, while the hole deposited by TiO$_2$ without TMPMCT almost was closed off with the formation of a seam, no pinch-off was observed for 40 s and 60 s TMPMCT exposure samples. The gradient blocking property was consistent for other sampling points in the same 8-inch wafer (TEM images in Supplementary Fig. 9). The thicknesses of TiO$_2$ on the 40 s sample were distributed from 10 nm to 30 nm (blue points in Fig. 4b). The thicknesses of the 60 s sample were distributed more widely, from 2 nm to 30 nm with changing depth (orange points in Fig. 4b). In addition, the 40 s TMPMCT with H$_2$O samples exhibited a thickness distribution similar to that of the 60 s TMPMCT sample without H$_2$O. Near the opening, the blocking property of the longer exposure sample was more significant than that of the shorter exposure sample, similar to those on planar samples. The selectivity (Fig. 4c) of the 60 s sample was almost 90% at the top of the hole but decreased to 20% with increasing depth. The two 40 s samples with and without H$_2$O also exhibited selectivity changes.

Because 3D nanostructures possess a much larger surface area than 2D planar surfaces, the adsorption behaviour on both structures should be different under the same exposure conditions, leading to different molecular adsorption densities. To quantify the results, we adopted a kinetic model to estimate the adsorption density of TMPMCT inside 3D nanoscale holes. The time t (s), which is required to cover the surface area of a 3D hole down to the depth λ (nm) can be calculated by the following equation (details in Supplementary Note 3)[39]:

$$t = \int_0^t dt = \frac{Q\sqrt{2\pi m k T}}{P} \frac{p}{A_{hole}} \int_0^L d\lambda \left(1 + \frac{3p\lambda}{16A_{hole}}\right)$$

Although a perfectly cylinder-shaped hole was not used for this experiment, it can provide a good explanation for the approximate adsorption density changes. Figure 4d shows a plot of relative coverage of TMPMCT with different pulses versus the hole depth, calculated from the above-mentioned equation. The molecular adsorption on the top area is faster than that inside the hole because more time is required for molecules to reach the lower portion of the hole (Fig. 4e, f). Therefore, the relative coverage of TMPMCT was the highest at the top (depth = 0 nm) and decreased with increasing depth for all TMPMCT pulses. The longest TMPMCT pulse, 60 s, resulted in higher relative coverage at the top than the 40 s and 20 s TMPMCT pulses. As a result, the application of a short TMPMCT pulse would narrow the relative-coverage distribution. Therefore, more exposure time is required to cover a surface deeper inside the hole because of the geometrically limited flux of the inhibitor molecule. In other words, under constant exposure conditions, the adsorption density of TMPMCT should change with the changing depth, as plotted. Because the adsorption density of TMPMCT is

a   100 nm TiO₂ ALD/SiO₂ hole without TMPMCT

b   100 nm TiO₂ ALD/60 s TMPMCT/SiO₂ hole

Top-down TEM images at different depth

- Top–down TEM images: holes are cut at different depths (0–1400 nm).
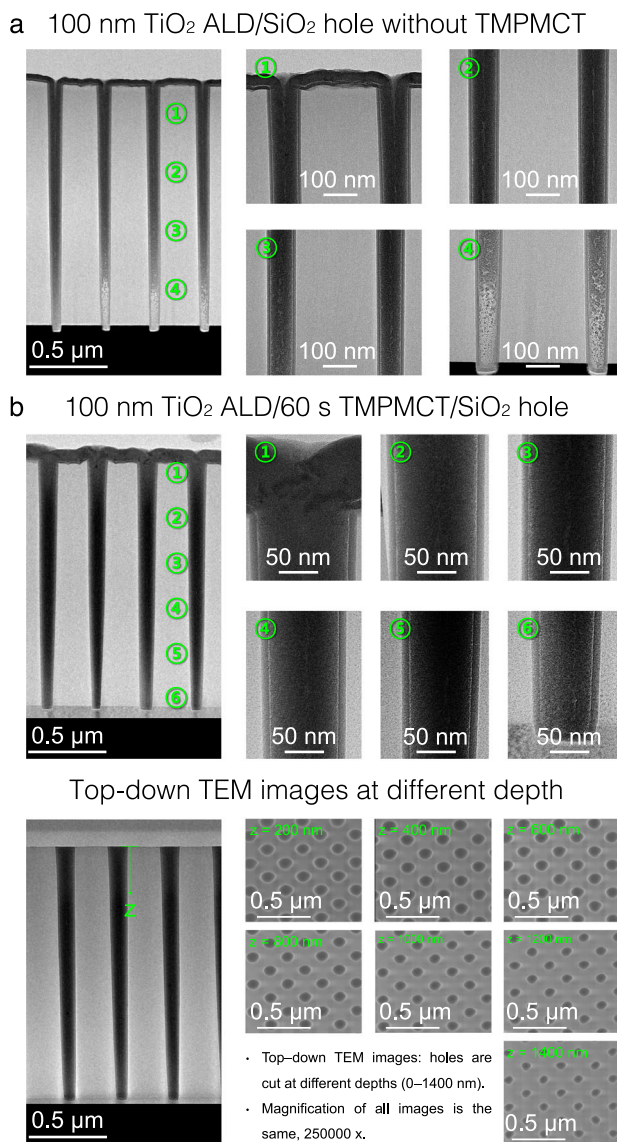- Magnification of all images is the same, 250000 x.

Fig. 5 | 100 nm TiO₂ ALD deposited in holes with and without TMPMCT inhibitor. a Cross-sectional TEM images of the hole pattern (depth = 1600 nm) for 100 nm TiO₂ ALD without TMPMCT. Unfilled zones are observed at the bottom (zone 4), and seam formation occurs along the centreline of the hole (zones 2 and 3). **b** Cross-sectional TEM images of the 100 nm TiO₂ ALD/60 s TMPMCT/SiO₂ hole and top-down TEM images at different depths, demonstrating hole filling without any seam formation.

proportional to the blocking property and selectivity, the relative coverage as a function of depth should be similar to the selectivity as a function of depth. Compared with Fig. 4c, plots resulting from the kinetic model demonstrate a high consistency, indicating that the blocking property changes depending on geometrical factors.

Based on this interpretation, we also performed a gradient ASD for seamless deposition on 8-inch wafers in a production-scale system (Supplementary Fig. 8). Figure 5a indicates that it is not feasible to fill the high-aspect-ratio hole (depth = 1600 nm) perfectly using 100 nm TiO₂ ALD without TMPMCT. Cross-sectional TEM images show an unfilled zone and seam formation along the centreline of the hole. In addition, the seam formation significantly varied with the position in the wafer; thus, large voids were observed in the non-uniform regions of the wafer (TEM image in Supplementary Fig. 10 and uniformity data in Supplementary Table 4). Furthermore, when 60 s TMPMCT was used, perfect filling was observed without any seam or void formation,

as shown in the cross-sectional and top-down TEM images acquired at different depths (Fig. 5b). Energy-dispersive spectroscopy (EDS) mapping (Supplementary Fig. 11) revealed that only Si, Ti and O were present without any significant amount of C. In addition, the results of the EDS line profile across the ASD TiO₂/TMPMCT/SiO₂ hole sample (Supplementary Fig. 12) demonstrate that no significant carbon impurities were left by TMPMCT between the substrate and TiO₂, even after the cessation of the blocking property (Supplementary Fig. 12b). TMPMCT should exist in a Cp(CH₃)₅Ti form after ASD TiO₂ (DFT results in Fig. 2a), forming Ti−C impurities; however, only a negligible amount of C was detected within the limits of the measurement (Supplementary Fig. 12d).

Discussion

We proposed a Ti precursor inhibitor, TMPMCT, and studied its chemical and physical adsorption behaviour by using theoretical methods, DFT and MC simulations. The degradation of the TiO₂ blocking property with an increasing number of ALD cycles was investigated by adopting an MC simulation and a kinetic growth model, the JMAK equation. It was revealed that the unoccupied sites in the inhibitor layer play an important role in the degradation of ASD TiO₂ films, and the blocking property could be controlled by adjusting the surface coverage of the inhibitor. To improve the blocking property, an additional H_2O pulse was added, as suggested by theoretical calculations and evaluation by DFT and MC simulation. H_2O was found to eliminate the OMe ligands of the adsorbed TMPMCT, creating more space for additional adsorption of TMPMCT. A monolayer of the TMPMCT inhibitor was found to block a 45 nm thick TiO₂ thin film in the subsequent ALD process, which is the thickest film thickness ever reported to date. In addition, the TMPMCT inhibitor with an H_2O pulse demonstrated a significantly improved blocking property up to 49 nm of TiO₂ blocking.

In 3D nanoscale hole patterns, ASD TiO₂ films exhibited a geometrically anisotropic growth. By adopting a kinetic model, the adsorption behaviour of a TMPMCT inhibitor inside 3D holes was interpreted. The adsorption density of the inhibitor was found to vary inside the 3D holes because of the geometrically limited flux, leading to a gradient ASD. A perfectly seamless TiO₂ deposition was obtained in the nanoscale 3D holes through ASD. Because the gradient ASD process works based on the fundamentals of molecular chemical and physical behaviours, this approach can be applied to other material systems in ALD. In addition, the experiments were repeated many times with a large number of samples on a production-scale system. The results were used for plotting graphs; parameters such as thickness and selectivity were averaged from different runs, and their standard deviations were determined (Supplementary Table 4 and Supplementary Fig. 14). The gradient ASD approach proposed herein has high reliability because it can be reproduced and applied to a large-scale ALD system. Hence, the fundamental understandings derived from this study can be directly applicable at manufacturing scales.

Methods

Sample preparation

Experiments were conducted on a lab-scale ALD machine (Atomic-Shell, CN1 Co., Korea) and scaled to a high volume production by a spatial-divided ALD (SALD) machine at the Samsung Advanced Institute of Technology. The SALD system includes an 8-inch rotary chamber that features a 16-split shower head with individual nozzle control. The susceptor rotates at 40 rpm, and the chamber can load three 8-inch wafers simultaneously, as shown in Supplementary Fig. 8. In the lab-scale ALD system, a small coupon wafer was loaded, and the precursor and counter-reactant were dosed on to the wafer via a nozzle line. Additional information on the lab-scale ALD system can be found in refs. 12, 40, 41.

The TiO₂ precursors, titanium isopropoxide (TTIP) (Sigma-Aldrich) and tetrakis-(dimethylamido)titanium (TDMAT) (Oceanbridge Co., Ltd,

Korea), were contained in a canister at 50 °C. The H_2O reactant was kept at 25 °C. Trimethoxy-(pentamethylcyclopentadienyl)titanium(IV) $(Cp(CH_3)_5Ti(OMe)_3)$, abbreviated as TMPMCT (Ichems Co., Korea), was used as an inhibitor and was investigated at different temperatures. The substrates used in these experiments included a planar SiO_2 wafer and hole patterns (1600 nm depth, 100 nm diameter opening, 50 nm bottom diameter). They were sequentially cleaned using acetone, isopropyl alcohol and deionised water and dried using N_2 flow.

All experiments were performed at 180 °C[42–46]. The GPCs were approximately 0.40 and 0.55 Å/cycle for TTIP and TDMAT precursors, respectively (Supplementary Fig. 1a–d). The adsorption mechanism of the TMPMCT inhibitor on the TiO_2 surface was investigated at different adsorption times (20–60 s) and canister temperatures (70–100 °C) (Supplementary Fig. 1e and f). The adsorption mechanism of the TMPMCT inhibitor on various substrates, namely, TiO_2-deposited SiO_2, Ru-deposited SiO_2, HfO_2-deposited SiO_2, TiN and SiO_2, was also investigated; the results are shown in Supplementary Fig. 1g. The TMPMCT inhibitor layer was used to evaluate the blocking property against TiO_2 ALD on SiO_2 and 10 nm TiO_2-deposited SiO_2 substrates, as shown in Supplementary Fig. 2. The results show that the TiO_2 ALD thin films were obtained on the bare surfaces, but no TiO_2 growth was observed on the TMPMCT-inhibited surfaces. The blocking property of the TMPMCT was examined at 20, 40 and 60 s exposure on TiO_2-deposited SiO_2 substrate, against 1000 cycles of TiO_2 ALD. An additional H_2O pulse was included to improve the coverage and blocking property of TMPMCT by inserting an H_2O pulse to interrupt the continuous TMPMCT pulse. The sequence followed was TMPMCT pulse–additional H_2O pulse–TMPMCT. In the gradient ASD experiments, we used an SiO_2 hole pattern with a 1600 nm depth, 100 nm opening diameter and 50 nm bottom diameter. Before TMPMCT exposure, a 10 nm TiO_2 was deposited on the SiO_2 hole patterns to produce a TiO_2 surface; hence, the opening diameter was reduced from 100 nm to 80 nm. We then investigated 20, 40 and 60 s of TMPMCT exposure and 40 s of TMPMCT with H_2O pulses in the gap-filling processing of 40 nm and 100 nm TiO_2.

Sample characterization
The thickness of the deposited films was measured using field-emission scanning electron microscopy (FE-SEM; JEOL JSM-7001F; JEOL, Ltd.), which included ellipsometry at an incidence angle of 64.885° for thicknesses between 245 and 1000 nm (i.e., from −1.24 to 5.06 eV), and high-resolution transmission electron microscopy (JEM-2100F, JEOL) equipped with an energy-dispersive X-ray spectroscopy and a 50 nm² probe (solid angle = 0.28 sr, take-off angle = 24.1°), as shown in Figs. 4, 5, and Supplementary Figs. 9, 10, 11, 12.

Theoretical calculations
DFT calculations were performed using the Vienna ab initio simulation package version 5.4.4[47]. Within the DFT + U framework, the Perdew–Burke-Ernzerhof generalised gradient approximation functional was employed to treat the exchange-correlation energy[48] while applying the D3(BJ) dispersion correction[49]. Using Dudarev's approximation[50], parameter U_{eff} (=U − J) for Ti was set to 3, which is an optimised value from the literature[51]. A clean anatase TiO_2 (101) surface was used to simulate surface reactions. ALD-grown TiO_2 was reported to exist in the anatase phase at a considered temperature in this study[41,52], and the lowest surface energy was in the (101) plane[53]. Most H_2O and OH moieties desorb from the anatase TiO_2(101) surface at temperatures above 400 K[54]. The first surface model, a three-layered TiO_2 surface with dimensions of $10.5 \times 11.4 \times 28$ Å, was used to locate local or global minimum structures while the forces acting on the atoms were less than 0.02 eV Å⁻¹. Energy barriers were obtained via the nudged elastic band method with a force tolerance of 0.05 eV Å⁻¹ [55,56]. The $Cp(CH_3)_5$Ti-terminated surface was simulated using the second surface model, two-layered TiO_2 surface ($20.9 \times 11.4 \times 28$ Å), with a

force tolerance of 0.02 eV Å⁻¹. The surface models contained more than 10 Å of the vacuum region. All calculations were conducted with an energy cut-off level of 500 eV. A $2 \times 2 \times 1$ k-point grid for the surface models was set according to the Monkhorst–Pack scheme after convergence test. The adsorption energy (E_{ad}) was defined as $E_{ad} = E_{total} - (E_{slab} + E_{molecule})$, where E_{total} and E_{slab} are the total electronic energies of the slab with and without an adsorbate, respectively, and $E_{molecule}$ is the energy of the gaseous molecule.

The physical adsorption, the coverage of TMPMCT on the TiO_2 surface, and the elimination of OMe ligands of TMPMCT using H_2O were investigated via MC simulations. The MC simulations were performed using a modified algorithm, which was run on the simulation programme "R" (version 3.6.1; GUI 1.70; EL Capitan build 7684). Further information can be found in our previous reports[8,12] (algorithm in Supplementary Fig. 13). We also employed the Johnson–Mehl–Avrami–Kolmogorov (JMAK) model to quantify the blocking property and degradation with experimental data[4,35,36]. The JMAK model was calculated using the Matlab software (Matlab R2018b version 9.5). In addition, the adsorption density of TMPMCT inside a 3D nanoscale hole was calculated using various TMPMCT pulses of 20, 40 and 60 s.

Data availability
The data that support the findings of this study are available from the corresponding authors upon reasonable request. Source data are provided with this paper.

References
1. Johnson, R. W., Hultqvist, A. & Bent, S. F. A brief review of atomic layer deposition: from fundamentals to applications. *Mater. Today* **17**, 236–246 (2014).
2. Cremers, V., Puurunen, R. L. & Dendooven, J. Conformality in atomic layer deposition: current status overview of analysis and modelling. *Appl. Phys. Rev.* **6**, 021302 (2019).
3. Kim, H., Lee, H.-B.-R. & Maeng, W.-J. Applications of atomic layer deposition to nanofabrication and emerging nanodevices. *Thin Solid Films* **517**, 2563–2580 (2009).
4. Lee, H.-B.-R., Mullings, M. N., Jiang, X., Clemens, B. M. & Bent, S. F. Nucleation-controlled growth of nanoparticles by atomic layer deposition. *Chem. Mater.* **24**, 4051–4059 (2012).
5. Kim, Y. R. et al. Fluorine-containing polymeric inhibitor for highly selective and durable area-selective atomic layer deposition. *Appl. Surf. Sci.* **578**, 152056 (2022).
6. Kim, W.-H. et al. A process for topographically selective deposition on 3D nanostructures by ion implantation. *ACS Nano* **10**, 4451–4458 (2016).
7. Pattison, T. G. et al. Surface initiated polymer thin films for the area selective deposition and etching of metal oxides. *ACS Nano* **14**, 4276–4288 (2020).
8. Khan, R. et al. Area-selective atomic layer deposition using Si precursors as inhibitors. *Chem. Mater.* **30**, 7603–7610 (2018).
9. Mameli, A. et al. Area-selective atomic layer deposition of SiO_2 using acetylacetone as a chemoselective inhibitor in an ABC-type cycle. *ACS Nano* **11**, 9303–9311 (2017).
10. Mackus, A. J. M., Merkx, M. J. M. & Kessels, W. M. M. From the bottom-up: toward area-selective atomic layer deposition with high selectivity. *Chem. Mater.* **31**, 2–12 (2019).
11. Minaye Hashemi, F. S., Prasittichai, C. & Bent, S. F. Self-correcting process for high quality patterning by atomic layer deposition. *ACS Nano* **9**, 8710–8717 (2015).
12. Kim, H. G. et al. Effects of Al precursors on deposition selectivity of atomic layer deposition of Al_2O_3 using ethanethiol inhibitor. *Chem. Mater.* **32**, 8921–8929 (2020).
13. Talukdar, T. K., Girolami, G. S. & Abelson, J. R. Seamless fill of deep trenches by chemical vapor deposition: use of a molecular growth

inhibitor to eliminate pinch-off. *J. Vac. Sci. Technol. A* **37**, 021509 (2019).

14. Talukdar, T. K., Wang, W. B., Girolami, G. S. & Abelson, J. R. Superconformal coating and filling of deep trenches by chemical vapor deposition with forward-directed fluxes. *J. Vac. Sci. Technol. A* **36**, 051513 (2018).

15. Abdolvand, R., Johari, H., Ho, G. K., Erbil, A. & Ayazi, F. Quality factor in trench-refilled polysilicon beam resonators. *J. Microelectromechanical Syst.* **15**, 471–478 (2006).

16. Schenk, H., Dürr, P., Kunze, D., Lakner, H. & Kück, H. A resonantly excited 2D-micro-scanning-mirror with large deflection. *Sens. Actuators A: Phys.* **89**, 104–111 (2001).

17. Sun, M. et al. Efficient visible light modulation based on electrically tunable all dielectric metasurfaces embedded in thin-layer nematic liquid crystals. *Sci. Rep.* **9**, 8673 (2019).

18. Kim, W. et al. Thermally-curable nanocomposite printing for the scalable manufacturing of dielectric metasurfaces. *Microsyst. Nanoeng.* **8**, 73 (2022).

19. Choudhury, S. M. et al. Material platforms for optical metasurfaces. *Nanophotonics* **7**, 959–987 (2018).

20. Wu, Y., Yang, W., Fan, Y., Song, Q. & Xiao, S. TiO$_2$ metasurfaces: from visible planar photonics to photochemistry. *Sci. Adv.* **5**, eaax0939 (2019).

21. Langereis, E., Roijmans, R., Roozeboom, F., van de Sanden, M. C. M. & Kessels, W. M. M. Remote plasma ALD of SrTiO$_3$ using cyclopentadienyl-based Ti and Sr precursors. *J. Electrochem. Soc.* **158**, G34 (2011).

22. Rose, M. et al. Atomic layer deposition of titanium dioxide thin films from Cp*Ti(OMe)$_3$ and ozone. *J. Phys. Chem. C.* **113**, 21825–21830 (2009).

23. Zydor, A. & Elliott, S. D. TiCp*(OMe)$_3$ versus Ti(OMe)$_4$ in atomic layer deposition of TiO$_2$ with water—ab initio modelling of atomic layer deposition surface reactions. *J. Nanosci. Nanotech.* **11**, 8089–8093 (2011).

24. Zydor, A., Kessler, V. G. & Elliott, S. D. First principles simulation of reaction steps in the atomic layer deposition of titania: dependence of growth on Lewis acidity of titanocene precursor. *Phys. Chem. Chem. Phys.* **14**, 7954–7964 (2012).

25. Zydor, A. & Elliott, S. D. Thermal stability of precursors for atomic layer deposition of TiO$_2$, ZrO$_2$, and HfO$_2$: an ab initio study of α-hydrogen abstraction in bis-cyclopentadienyl dimethyl complexes. *J. Phys. Chem. A* **114**, 1879–1886 (2010).

26. Niinistö, J. et al. Novel mixed alkylamido-cyclopentadienyl precursors for ALD of ZrO$_2$ thin films. *J. Mater. Chem.* **18**, 5243 (2008).

27. Miyauchi, M., Nakajima, A., Watanabe, T. & Hashimoto, K. Photocatalysis and photoinduced hydrophilicity of various metal oxide thin films. *Chem. Mater.* **14**, 2812–2816 (2002).

28. Fujishima, A., Zhang, X. & Tryk, D. A. TiO$_2$ photocatalysis and related surface phenomena. *Surf. Sci. Rep.* **63**, 515–582 (2008).

29. Levrau, E. et al. Atomic layer deposition of TiO$_2$ on surface modified nanoporous low-k films. *Langmuir* **29**, 12284–12289 (2013).

30. Haider, A., Yilmaz, M., Deminskyi, P., Eren, H. & Biyikli, N. Nanoscale selective area atomic layer deposition of TiO$_2$ using e-beam patterned polymers. *RSC Adv.* **6**, 106109–106119 (2016).

31. Nguyen, C. T. et al. Atomic layer modulation of multicomponent thin films through combination of experimental and theoretical approaches. *Chem. Mater.* **33**, 4435–4444 (2021).

32. Gladfelter, W. L. Selective metalization by chemical vapor deposition. *Chem. Mater.* **5**, 1372–1388 (1993).

33. Puurunen, R. L. & Vandervorst, W. Island growth as a growth mode in atomic layer deposition: a phenomenological model. *J. Appl. Phys.* **96**, 7686–7695 (2004).

34. Guo, L., Oskam, G., Radisic, A., Hoffmann, P. M. & Searson, P. C. Island growth in electrodeposition. *J. Phys. D: Appl. Phys.* **44**, 443001 (2011).

35. Parsons, G. N. Functional model for analysis of ALD nucleation and quantification of area-selective deposition. *J. Vac. Sci. Technol. A* **37**, 020911 (2019).

36. Avrami, M. Kinetics of phase change. II Transformation-time relations for random distribution of nuclei. *J. Chem. Phys.* **8**, 212–224 (1940).

37. Ko, B. G. et al. Growth modulation of atomic layer deposition of HfO$_2$ by combinations of H$_2$O and O$_3$ reactants. *Dalton Trans.* https://doi.org/10.1039/D1DT03465K (2021).

38. Cho, Y., Kim, S. H., Kim, B. S., Kim, Y. & Jeon, W. Modulation of the adsorption chemistry of a precursor in atomic layer deposition to enhance the growth per cycle of a TiO$_2$ thin film. *Phys. Chem. Chem. Phys.* **23**, 2568–2574 (2021).

39. Gordon, R. G., Hausmann, D., Kim, E. & Shepard, J. A kinetic model for step coverage by atomic layer deposition in narrow holes or trenches. *Chem. Vap. Depos.* **9**, 73–78 (2003).

40. Nguyen, C. T., Yoon, J., Khan, R., Shong, B. & Lee, H.-B.-R. Thermal atomic layer deposition of metallic Ru using H$_2$O as a reactant. *Appl. Surf. Sci.* **488**, 896–902 (2019).

41. Heikkilä, M., Puukilainen, E., Ritala, M. & Leskelä, M. Effect of thickness of ALD grown TiO$_2$ films on photoelectrocatalysis. *J. Photochemistry Photobiol. A: Chem.* **204**, 200–208 (2009).

42. Xie, Q. et al. Growth kinetics and crystallization behavior of TiO$_2$ films prepared by plasma enhanced atomic layer deposition. *J. Electrochem. Soc.* **155**, H688 (2008).

43. Gonzalez-Ramirez, J. D., Villicañamendez, M., Tiznado, H., Alonso-Nuñez, G. & Cortes, J. A. Atomic layer deposition of TiO$_2$ from tetrakis (dimethylamino) titanium and H$_2$O on commercial-grade iron: a simple method for support preparation. *Int. Referee. J. Eng. Sci.* **7**, 01–11 (2018).

44. Zhuiykov, S. et al. Wafer-scale fabrication of conformal atomic-layered TiO$_2$ by atomic layer deposition using tetrakis (dimethylamino) titanium and H$_2$O precursors. *Mater. Des.* **120**, 99–108 (2017).

45. Reinke, M., Kuzminykh, Y. & Hoffmann, P. Surface kinetics of titanium isopropoxide in high vacuum chemical vapor deposition. *J. Phys. Chem. C.* **119**, 27965–27971 (2015).

46. Filipovic, L. Modeling and simulation of atomic layer deposition. In *2019 International Conference on Simulation of Semiconductor Processes and Devices (SISPAD)* 1–4 (IEEE, 2019).

47. Kresse, G. & Furthmüller, J. Efficient iterative schemes for ab initio total-energy calculations using a plane-wave basis set. *Phys. Rev. B* **54**, 11169–11186 (1996).

48. Perdew, J. P., Burke, K. & Ernzerhof, M. Generalized gradient approximation made simple. *Phys. Rev. Lett.* **77**, 3865–3868 (1996).

49. Grimme, S., Ehrlich, S. & Goerigk, L. Effect of the damping function in dispersion corrected density functional theory. *J. Computational Chem.* **32**, 1456–1465 (2011).

50. Dudarev, S. L., Botton, G. A., Savrasov, S. Y., Humphreys, C. J. & Sutton, A. P. Electron-energy-loss spectra and the structural stability of nickel oxide: an LSDA+U study. *Phys. Rev. B* **57**, 1505–1509 (1998).

51. Hu, Z. & Metiu, H. Choice of *U* for DFT+*U* calculations for titanium oxides. *J. Phys. Chem. C.* **115**, 5841–5845 (2011).

52. Cheng, H.-E. & Chen, C.-C. Morphological and photoelectrochemical properties of ALD TiO$_2$ films. *J. Electrochem. Soc.* **155**, D604 (2008).

53. Lazzeri, M., Vittadini, A. & Selloni, A. Structure and energetics of stoichiometric TiO$_2$ anatase surfaces. *Phys. Rev. B* **63**, 155409 (2001).

54. Walle, L. E. et al. Mixed dissociative and molecular water adsorption on anatase TiO$_2$ (101). *J. Phys. Chem. C.* **115**, 9545–9550 (2011).

55. Henkelman, G., Uberuaga, B. P. & Jónsson, H. A climbing image nudged elastic band method for finding saddle points and minimum energy paths. *J. Chem. Phys.* **113**, 9901–9904 (2000).

56. Henkelman, G. & Jónsson, H. Improved tangent estimate in the nudged elastic band method for finding minimum energy paths and saddle points. *J. Chem. Phys.* **113**, 9978–9985 (2000).

Author contributions

H.-B.-R.L. initially conceptualized and designed the project. C.T.N. and E.-H.C. carried out all sample synthesis and characterization. C.T.N. wrote the manuscript. B.G. calculated the MC simulation. B.S., J.P. and N.-K.Y. calculated the DFT results and wrote this part. S.S. calculated the gradient adsorption of precursors. S.L., H.-S.K. and J.Y.L. performed the analyses. All authors contributed to the overall scientific interpretation and revised this paper.

Competing interests

The authors declare no competing interests.

Additional information

Supplementary information The online version contains supplementary material available at https://doi.org/10.1038/s41467-022-35428-6.

Correspondence and requests for materials should be addressed to Han-Bo-Ram Lee.

Peer review information *Nature Communications* thanks Sean Barry and the other, anonymous, reviewer(s) for their contribution to the peer review of this work.

Reprints and permissions information is available at http://www.nature.com/reprints

Publisher's note Springer Nature remains neutral with regard to jurisdictional claims in published maps and institutional affiliations.